

Multi Messenger Study of GRB 221009A with VHE Gamma-ray and Neutrino Afterglow from a Gaussian Structured Jet

Tanima Mondal^a, Soebur Razzaque^{b,c,d}, Jagdish C. Joshi^{e,b}, Sonjoy Majumder^f, Debanjan Bose^g

^aDepartment of Physics, Indian Institute of Technology Kharagpur, Kharagpur, West Bengal, 721302, India

^bCentre for Astro-Particle Physics (CAPP) and Department of Physics, University of Johannesburg, PO Box 524, Auckland Park, 2006, South Africa

^cDepartment of Physics, George Washington University, , Washington, DC 20052, USA

^dNational Institute for Theoretical and Computational Sciences (NITheCS), Private Bag XI, Matieland, , South Africa

^eAryabhata Research Institute of Observational Sciences, Manora Peak, Nainital, 263129, India

^fDepartment of Physics, Indian Institute of Technology Kharagpur, , Kharagpur, 721302, West Bengal, India

^gDepartment of Physics, Central University of Kashmir, , Ganderbal, 191131, Jammu & Kashmir, India

Abstract

Recent detections of very-high-energy (VHE; ≥ 100 GeV) emission from GRB afterglows, most notably the unprecedented brightness of GRB 221009A observed by LHAASO, reveal emission components beyond the standard electron synchrotron model. The multi-TeV photons motivate synchrotron self-Compton and possibly hadronic contributions, while the non-detection of coincident neutrinos by IceCube/KM3NeT/GRAND200k constrains the microphysical parameters, jet kinetic energy and ambient medium density. We model the VHE afterglow of GRB 221009A with an external forward shock from a Gaussian structured jet in a uniform density medium. This angular structure reproduces the extreme TeV output at an off-axis angle but without demanding large energies as in a top-hat jet. We also compute the corresponding $p\gamma$ neutrino flux in the PeV-EeV energies and derive a time-integrated upper limit based on the effective area of IceCube Gen2 and GRAND200k. This provides us with insights into the contributions of individual GRBs to the neutrino events. The predicted neutrino flux for GRB 221009A with model parameters inferred from multi-wavelength spectral energy distribution lies below the sensitivities of these detectors. Even our correlation analysis, optimized to search for neutrino signals by the upcoming GRAND200k, infers that the events from this GRB are of order ~ 0.1 under a highly optimistic microphysical parameter regime. We also compare the variation in neutrino flux arising from on-axis and off-axis jet viewing geometries, and conclude that it can account for approximately an order of magnitude difference in the neutrino signal. Thus, our studies conclude that a brighter burst occurring closer than GRB 221009A would be crucial for any neutrino detections by upcoming neutrino telescopes. Future GRB detections by the Cherenkov Telescope Array will provide important constraints on their geometry, radiation mechanisms, and any potential associated neutrino signals.

Keywords: GRBs, Afterglows, Neutrinos, Multi Messenger

1. Introduction

Gamma-ray bursts (GRBs) are one of the most energetic explosions in the Universe, and their broadband afterglow emission, from radio waves to very-high-energy (VHE) γ -rays, is well described by synchrotron radiation produced by relativistic electrons accelerated in external shocks (Mészáros and Rees, 1997; Costa et al., 1997; van Paradijs et al., 1997; Frail et al., 1997; Sari et al., 1998; Lloyd and Petrosian, 2000; Burgess et al., 2020). In recent years, detections of GeV–TeV emission by ground-based Cherenkov telescopes (MAGIC Collaboration, 2019; HESS Collaboration, 2019, 2021; LHAASO collaboration, 2023; MAGIC Collaboration, 2024) have revealed radiation components beyond the standard synchrotron model. Proposed mechanisms include synchrotron self-Compton (SSC) scattering, where relativistic electrons upscatter their own synchrotron photons to TeV energies (Chiang and Dermer, 1999; Dermer et al., 2000; Sari and Esin, 2001; Murase et al., 2011; Fraija et al., 2019; Wang et al., 2019; Derishev and Piran, 2019; Joshi and Razzaque, 2021; Mondal et al., 2023; Ren et al., 2024a);

proton-synchrotron emission from ultra-relativistic protons (Israel et al., 2023); and photo-hadronic ($p\gamma$) interactions producing electromagnetic cascades and high energy neutrinos (Razzaque, 2010, 2013; Sahu et al., 2022). These processes provide a plausible probe of both the particle acceleration efficiency and the microphysical conditions in GRB blast waves, while also linking GRBs to the broader context of ultra-high-energy cosmic rays (UHECRs) and neutrinos (Waxman, 1995; Vietri, 1995).

GRBs are considered as potential sources of UHECR acceleration. Detecting ultra-high energy (UHE) (\geq PeV) neutrinos from them would serve as a direct way to assess their role in UHECR production. Within the fireball framework of GRB jets, high energy neutrinos can be produced in multiple interaction scenarios. In internal shocks, neutrinos may arise from interactions of shock-accelerated cosmic-ray protons with prompt photons (Waxman and Bahcall, 1997). Later, in the external forward shocks of the blast wave, non-thermal protons interacting with afterglow photons can generate TeV–PeV neutrinos (Waxman and Bahcall, 2000; Razzaque, 2013; Razzaque and

Yang, 2015). In addition, the external reverse shock has been proposed as an efficient site for the acceleration of UHECRs, leading to the possible production of EeV neutrinos (Murase, 2007).

The current generation neutrino detector, IceCube, reported more than one hundred VHE astrophysical neutrinos through the High-Energy Starting Events (HESE) catalogue (Aartsen et al., 2020; Abbasi et al., 2021, 2022), along with 276 events through the IceCube Event catalogue of Alert Tracks (Abbasi et al., 2023b). However, despite extensive stacking analyzes of hundreds of GRBs and dedicated follow-ups of exceptionally bright events such as GRB 080319B, GRB 130427A, GRB 160625B, and GRB 221009A, no significant neutrino associations have been found with GRBs, either during prompt emission or in the afterglow phases (Abbasi et al., 2023a).

On 9 October 2022, at 13:16:59 UT (T_0), the Gamma-ray Burst Monitor (GBM) on board *Fermi* detected GRB 221009A, an exceptionally luminous and nearby ($z \sim 0.151$) long-duration GRB (de Ugarte Postigo et al., 2022; Veres et al., 2022). The burst was subsequently observed by several instruments, including *Swift* (Williams et al., 2023), *Fermi-LAT* (Lesage et al., 2023; Banerjee et al., 2025), INTEGRAL/SPI-ACS, and Konus-Wind (Frederiks et al., 2023), with its localization refined through InterPlanetary Network triangulation (Svinkin et al., 2022). Among the extensive multiwavelength and multi messenger follow-ups, a particularly remarkable discovery was the detection of photons with energies exceeding 10 TeV, reported by LHAASO (LHAASO collaboration, 2023; Huang et al., 2022), marking the first ultra-high-energy γ -ray observation from a long GRB.

The large isotropic kinetic energy and relatively close distance make GRB 221009A a promising target for high-energy neutrino detection. Being the brightest-of-all-time (BOAT) event, it offers a rare opportunity to probe neutrino production in GRB jets and to test the efficiency of hadronic processes in such extreme explosions. Several recent studies have explored the implications of IceCube’s non-detection of neutrinos from this burst by analysing its time-integrated γ -ray flux (Murase et al., 2022; Ai and Gao, 2023). This null result provides important constraints on the physical conditions of GRB outflows and places stringent limits on the allowed parameter space of emission models (Ai and Gao, 2023; Veres et al., 2024).

Different energy ranges of neutrino events require numerous analysis strategies in current detectors such as IceCube (Abbasi et al., 2023a) and KM3NeT (Aiello et al., 2019), which search for neutrino emission from astrophysical transients like GRBs over broad energy and temporal intervals. For GRB 221009A, the IceCube Collaboration conducted a dedicated search using its real-time Fast Response Analysis (FRA), optimized for TeV–PeV neutrinos (IceCube Collaboration, 2022). The search was performed at a reference energy $E_0 = 100$ TeV during two time windows, $[T_0 - 1 \text{ hr}, T_0 + 2 \text{ hr}]$ and $[T_0 \pm 1 \text{ day}]$, and reported only upper limits on neutrino emission (Abbasi et al., 2023a). Within the three-hour window, IceCube set a 90% confidence-level upper limit on the time-integrated muon-neutrino flux of $E^2 dN/dE \leq 3.9 \times 10^{-2} \text{ GeV cm}^{-2}$ assuming an E^{-2} power-law spectrum, with a sensitivity range of approx-

imately 800 GeV–1 PeV¹. Similarly, the KM3NeT Observatory carried out a search in the interval $[T_0 - 50 \text{ s}, T_0 + 5000 \text{ s}]$ and also reported no evidence for neutrino emission (KM3NeT Collaboration, 2022; Aiello et al., 2024).

Several numerical studies have attempted to explain the origin of the TeV photons observed from GRB 221009A, invoking top-hat jet models with varying opening angles (Sato et al., 2023) or structured jets characterized by shallow power-law or Gaussian or two-component jet angular profiles (O’Connor et al., 2023; Gill and Granot, 2023; Zhang et al., 2024; Ren et al., 2024a). Such jet structures are expected to arise naturally from jet break through the progenitor star’s envelope or from cocoon formation during collapse (Lamb and Kobayashi, 2017; Gottlieb et al., 2018; Lazzati et al., 2018), and they strongly shape the observed afterglow emission through their angular energy and velocity distributions at different viewing angles. In our recent work (Mondal et al., 2025), we demonstrated that a Gaussian structured jet can successfully reproduce VHE off-axis afterglow emission and explored how afterglow parameters govern SSC light curves and TeV detectability with CTA. Building on this framework, in this study, we aim to investigate whether the Gaussian structured jet scenario can also account for the TeV photons of GRB 221009A, while extending the analysis to calculate the associated neutrino flux in a constant-density interstellar medium (ISM) with an adiabatically evolving forward shock. In particular, the impact of off-axis structured jets on the resulting neutrino flux remains poorly explored across the existing literature. In this work, we systematically investigate how both intrinsic and extrinsic jet parameters influence the neutrino flux and assess its detectability with current and upcoming observatories, such as IceCube Gen2 and GRAND200k. This approach enables us to identify the correlation among parameter regimes that strongly enhance the neutrino flux and increase the number of neutrino events towards the current upper limit of those neutrino detectors. This correlation study not only constrains the baryon loading and particle acceleration efficiency in GRB jets but also provides tighter constraints on parameters associated with the neutrino flux.

This paper is organized as follows. Section 2 describes the blast wave afterglow model with a Gaussian structured jet in a uniform ISM and computes the VHE γ -ray emission, including synchrotron and SSC components with Klein–Nishina, internal $\gamma\gamma$ attenuation, and EBL corrections. Section 3 investigates the parameter dependence of the VHE light curves, details the fitting methodology, and applies the model to GRB 221009A through spectral modeling and TeV afterglow light-curve analysis. Section 4 formulates the afterglow neutrino emission from the $p\gamma$ channel, and the impact of jet angular structure on the flavor-mixed neutrino flux at Earth. Section 5 presents the resulting constraints, comparing the predicted neutrino fluxes with IceCube Gen2 and GRAND200k upper limits. The section further explores a correlation study on key parameters that govern neutrino production and quantifies expected event yields within the GRAND200k sensitivity band. Finally, we conclude with a

¹<https://gcn.gsfc.nasa.gov/other/221009A.gcn3>

summary of the main results and their implications for GRB jet structure and multi messenger detectability.

2. VHE Afterglow from Gaussian Structured Jets

In this section, we present a Gaussian structured jet model to interpret the GeV–TeV afterglow emission of the BOAT GRB 221009A, as observed by LHAASO (LHAASO collaboration, 2023) and AGILE GRID (Foffano et al., 2024). By fitting these data, we constrain the jet structure, radiation mechanisms, and particle acceleration processes, thereby inferring the model parameters governing the VHE afterglow. Accurate modeling of the synchrotron and SSC components requires the evolution of both the nonthermal electron population and the downstream magnetic field. Previous studies (Mooley et al., 2018; Margutti et al., 2017) have shown that simple narrow top-hat jet models is insufficient to explain the VHE afterglow data. Their strong lateral expansion produces excessively steep post-peak declines and flux levels inconsistent with the observed late-time emission, restricting them to fitting only the early afterglow. Moreover, the top-hat assumption of uniform energy and Lorentz factor within a sharp half-opening angle, followed by an abrupt cut-off, requires unrealistically high isotropic-equivalent energies to explain the observed brightness, often exceeding plausible GRB energy budgets. Recent study by O’Connor et al. (2023) also explained the multiwavelength observation of this BOAT GRB with a shallow power-law angular profile ($\epsilon(\theta) \propto \theta^{-a}$ with $a < 2$), with both jet core and wing configuration, where they have shown that shallow power-law jets have the ability to avoid the energy crisis that would be caused by uniform jets (top-hat), and thus can capture the observed afterglow behaviour with a sharp jet-break. However, through their model, they have primarily explained the radio, optical- infrared (OIR), and late-time X-ray emission of different VHE bright GRBs, along with GRB 221009A. Further Gill and Granot (2023), also explain Xray and optical afterglow features of GRB 221009A with their shallow angular jet structure using the forward shock model. In one of our recent works, we already explored how a Gaussian Structured jet is efficient in producing VHE off-axis afterglow emission (Mondal et al., 2025). Thus, in this work, we adopt our VHE Gaussian structured jet model within the forward-shock adiabatic framework, which provides a typical explanation for both the extreme luminosity of GRB 221009A and its spectral and temporal evolution.

2.1. Blast wave modeling with Gaussian Structured jet

To model the VHE afterglow of GRB 221009A, we consider an external forward-shock scenario in which the relativistic ejecta interact with a uniform interstellar medium (ISM). For the jet dynamics, we employ the Gaussian structured-jet framework of Mondal et al. (2025). This framework naturally accounts for the temporal evolution of the afterglow through SSC emission, the dominant radiation mechanism responsible for the observed sub-TeV photons.

In the Gaussian structured jet model, jet energy per unit solid angle follows a Gaussian profile as (Lamb and Kobayashi, 2017),

$$\epsilon(\theta) = \frac{dE_k}{d\Omega} = \epsilon_c \exp\left(-\frac{\theta^2}{2\theta_c^2}\right), \quad (1)$$

where ϵ_c is the jet kinetic energy per unit solid angle at the jet core, characterized by the total kinetic energy E_k of the jet. The jet core angle θ_c shapes the jet structure, and $\theta_{j,max}$ is the maximum jet half-opening angle of the sharp-edge jet surface beyond which energy drops rapidly (see Section-4.3 for details). This angle does not have a significant impact on the total flux, since emission from low latitudes remains insignificant whenever the light curve lies above the detection threshold (Resmi et al., 2018). Along with the jet angular energy profile, jet initial velocity profile $\Gamma_0(\theta)\beta_0(\theta)$ also follows a Gaussian profile (Resmi et al., 2018; Mondal et al., 2025) as —

$$\Gamma_0(\theta)\beta_0(\theta) = \eta_c \exp\left(-\frac{\theta^2}{2\theta_c^2}\right), \quad (2)$$

Here $\Gamma_c\beta_c = \eta_c$ is constant, where Γ_c is jet core bulk Lorentz factor and β_c is the normalized velocity of the jet along Γ_c .

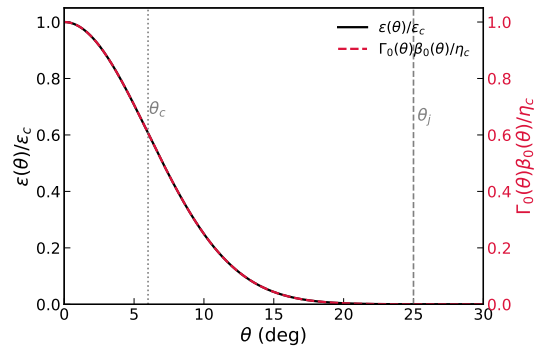


Figure 1: Normalized angular profiles of jet energy per unit solid angle, $\epsilon(\theta)/\epsilon_c$ (black solid line), and initial velocity, $\Gamma_0(\theta)\beta_0(\theta)/\eta_c$ (red dashed line), for a Gaussian structured jet. For example, the jet profile is shown as a function of the polar angle θ for a jet core angle $\theta_c = 6^\circ$, jet half-opening angle $\theta_{j,max} = 25^\circ$, initial velocity $\eta_c = 300$ and total kinetic energy $E_k = 1 \times 10^{53}$ erg. Vertical dotted and dashed lines mark θ_c and $\theta_{j,max}$, respectively.

Figure 1 illustrates both the angular profile of the energy and the bulk Lorentz factor gradually decrease from the jet core outward ($\theta > \theta_c$). Furthermore, since we assume adiabatic blast wave evolution of the bulk Lorentz factor for ultra-relativistic ejecta ($\Gamma\beta \gg 1$), the Blandford-McKee self-similar solution (Blandford and McKee, 1976) provides the radial evolution of the total bulk Lorentz as $\Gamma(\theta, r)\beta(\theta, r) \propto \left(\frac{r}{r_{dec}}\right)^{-3/2}$, for $r > r_{dec}$. Here, r is the radius of the blast wave from the center of explosion, r_{dec} is the deceleration radius that can be obtained as $r_{dec} = (3\epsilon_c/\eta_c^2 n_0 m_p c^2)^{1/3}$ (Mondal et al., 2025), with n_0 is number density of ambient medium, m_p is the mass of proton, c is velocity of light.

The temporal evolution of the afterglow is determined by jet intrinsic parameters — the total kinetic energy E_k , ambient density n_0 , jet core angle θ_c , the energy fractions in electrons (ϵ_e), magnetic fields (ϵ_B) and electron power law index k ; whereas the jet extrinsic parameters includes the viewing angle θ_v and

the luminosity distance d_L . In contrast to the typical top-hat jet scenario, a sharp jet break is expected in the temporal evolution, once the relativistic beaming angle becomes comparable to the jet opening angle (Sari et al., 1999). Our Gaussian structured jet model does not invoke an explicit jet-break time. The smooth angular energy distribution of the Gaussian profile naturally produces a gradual steepening of the afterglow light curve, consistent with the observed long-lived shallow decay of GRB 221009A, and alleviates the extreme energy requirements implied by a uniform jet with a late-time break (O'Connor et al., 2023).

2.2. Estimation of Synchrotron and SSC flux

In the Gaussian structured jet scenario, the early afterglow emission is dominated by synchrotron radiation from shock-accelerated non-thermal electrons (Wijers and Galama, 1999; Piran et al., 1998), which are accelerated following a characteristic power-law decay ($\propto \gamma^{-p}$) of energy distribution. In later times, sub-TeV photons are primarily produced by Synchrotron Self-Compton (SSC) scattering, where the same group of synchrotron electrons upscatter synchrotron photons to the VHE regime (Sari and Esin, 2001). The synchrotron spectrum is described by piecewise power-law segments separated by the minimum injection frequency ν_m , the cooling frequency ν_c^s and maximum frequency ν_M , associated with the electron Lorentz factors γ_m , γ_c^s and γ_M , respectively. Depending on the relative values of these Lorentz factors, the spectrum exhibits two cooling regimes: fast cooling ($\gamma_m > \gamma_c^s$) and slow cooling ($\gamma_c^s > \gamma_m$). At an early time of the afterglow, most of the electrons get efficiently cooled down within their dynamical timescale due to the strong magnetic field and high electron density. Whereas at a later time, when the blast wave expands, its comoving magnetic field weakens over time, and the electron cooling time dominates over the dynamical time. Hence, only the highest-energy electrons radiatively cool, having $\gamma > \gamma_c$. Furthermore, the maximum synchrotron Lorentz factor γ_M is calculated by comparing synchrotron acceleration and cooling time scale, beyond which electrons can not accelerate efficiently.

The relevant Lorentz factors and associated magnetic field strength are given by

$$\begin{aligned}\gamma_m &= \frac{m_p}{m_e} \left(\frac{p-2}{p-1} \right) \epsilon_e (\Gamma - 1) + 1, \\ \gamma_c &= \frac{6\pi m_e c (1+z)}{\sigma_T (1+Y) B^2 \Gamma t_{\text{ob}}}, \\ \gamma_M &= \sqrt{\frac{6\pi q_e e_{\text{acc}}}{\sigma_T B (1+Y)}}, \\ B &= \left(32\pi m_p c \Gamma^2 \epsilon_B n_0 \right)^{1/2},\end{aligned}$$

where σ_T is the Thomson cross-section and B is the comoving magnetic field strength. The Compton parameter Y describes the relative contribution of SSC cooling (Jacovich et al., 2021; Mondal et al., 2023), reducing the synchrotron cooling Lorentz factor and modifying the cooling break frequency.

Now, to compute the synchrotron flux, for an observer at a viewing angle θ_v from the jet axis, the apparent inclination angle $\alpha_{\text{inc}}^{i,k}$ of each segment relative to the line of sight is calculated following Resmi et al. (2018), where each segments defined by polar angles θ_i and azimuthal angles ϕ_k . Then, for those different jet segments, we calculate the deceleration radius r_{dec} of the fireball. For each of the (i,k) th segments, observer time t_{ob} is associated with its corresponding shock radius r and inclination angle $\alpha_{\text{inc}}^{i,k}$ Resmi et al. (2018); Mondal et al. (2025), i.e. $t_{\text{ob}}(r, \alpha_{\text{inc}}^{i,k}) = \frac{r}{\beta(r)c} \left[1 - \beta(r) \cos \alpha_{\text{inc}}^{i,k} \right]$. Thus, for a given range of r values, we have interpolated the $t_{\text{ob}}(r, \alpha_{\text{inc}}^{i,k}) - r$ equation to obtain off-axis flux contribution from each jet segment at a given t_{ob} . Hence, the total observed flux is obtained by summing the contributions from each jet segment at a given observer time. The observed synchrotron flux from each jet segment (i,k) is given by,

$$\begin{aligned}F_{\text{syn}}^{(i,k)}(t_{\text{ob}}, \alpha_{\text{inc}}^{i,k}) &= a_{\text{dop}}^3 F_{\nu/a_{\text{dop}}}^{i,k}(a_{\text{dop}} t, \alpha_{\text{inc}} = 0) \cos \alpha_{\text{inc}}^{i,k} \\ &= a_{\text{dop}}^3(r, \alpha_{\text{inc}}^{i,k}) \times \cos \alpha_{\text{inc}}^{i,k} \times P_{\nu, \text{max}} \\ &\quad \times \left(\frac{n_0}{3} \right) \times r^3 \times \frac{O_{\text{fact}}}{d_L^2} \times f_{\nu, \text{syn}} \\ &= a_{\text{dop}}^3(r, \alpha_{\text{inc}}^{i,k}) \times \cos \alpha_{\text{inc}}^{i,k} \times F_{\text{max, syn}}^{(i,k)} \times f_{\nu, \text{syn}}\end{aligned}\quad (3)$$

where $F_{\text{max, syn}}^{(i,k)}$ is maximum synchrotron peak flux which is primarily determined by peak-averaged power per unit frequency $P_{\nu, \text{max}} = m_e c^2 \sigma_T B \sqrt{\Gamma^2 + 1} / 3 q_e$ and the total number of electrons N_e present in each jet segment (Mondal et al., 2025). $f_{\nu, \text{syn}}$ represents normalized synchrotron spectral profile for slow and fast cooling regimes following Sari et al. (1998) and Zhang (2018). Further a_{dop} is the Doppler factor that accounts for the additional time to reach off-axis radiation to the observer compared to $t_{\text{obs}}(\alpha = 0)$ along the jet's central axis. O_{fact} represents the fraction of total jet solid angle associated with each discretized jet element (Resmi et al., 2018), ensuring that the total flux is obtained by summing the contributions from all angular jet segments. For each jetted element, $O_{\text{fact}} = \frac{\Omega_{i,k}}{\Omega_{e,i,k}}$, where $\Omega_{i,k} = \int_{\phi_{k-1}}^{\phi_k} d\phi \int_{\theta_{i-1}}^{\theta_i} d\theta \sin \theta$ is the solid angle subtended by a beamed element at a point on the central axis, and $\Omega_{e,i,k} = \max[\Omega_{i,k}, 2\pi(1 - \cos(1/\Gamma_{i,k}))]$ (Resmi et al., 2018). The term $\cos \alpha_{\text{inc}}^{i,k}$ represents accounts for the correction due to the emission area projection along the line of sight (Salmonson, 2003; Lamb and Kobayashi, 2017). Thus the above equation 3 represents the observed synchrotron flux contribution from each jet element, which can correspond to either on-axis ($\theta_c > \theta_v$) or off-axis ($\theta_v > \theta_c$) emission depending on the angular position of the segment.

Analogous to synchrotron emission, the SSC afterglow flux is governed by characteristic spectral break frequencies: the minimum injection frequency $\nu_{\text{mm}}^{\text{SSC}} = 2\nu_m \gamma_m^2$, the cooling frequency $\nu_{\text{cc}}^{\text{SSC}} = 2\nu_c \gamma_c^2$, and intermediate frequency $\nu_{\text{mc}}^{\text{SSC}} = \sqrt{\nu_{\text{mm}}^{\text{SSC}} \nu_{\text{cc}}^{\text{SSC}}}$. The cooling regime of the electron population is determined by the relative ordering of these frequencies — slow cooling

appears when $v_{mm}^{SSC} < v_{cc}^{SSC}$, while fast cooling occurs when $v_{mm}^{SSC} > v_{cc}^{SSC}$. The observed SSC flux from each jet segment can be calculated as —

$$\begin{aligned} F_{\text{SSC}}^{(i,k)} &= F_{\text{max,syn}}^{(i,k)} \times (n_0 r \sigma_T x_0) \times f_{v,\text{SSC}} \\ &= F_{\text{max,SSC}}^{(i,k)} \times f_{v,\text{SSC}} \end{aligned} \quad (4)$$

The SSC peak flux $F_{\text{max,SSC}}^{(i,k)}$ incorporates the synchrotron peak flux $F_{\text{max,syn}}^{(i,k)}$, the blast wave radius r , the ambient medium density n_0 , and the Thomson cross-section σ_T . This flux quantifies the efficiency of energy transfer from low-energy synchrotron photons to high-energy SSC photons. Thus, to obtain the afterglow flux evolution, both in synchrotron and SSC ($f_{v,\text{syn}}^{(i,k)}(t)$ and $f_{v,\text{SSC}}^{(i,k)}(t)$), it is crucial to estimate the time evolution of all break frequencies and peak specific flux. $f_{v,\text{SSC}}$ is the on-axis SSC spectrum profile for slow and fast cooling regimes, which further follows analytical approximation as given in Sari and Esin (2001) and Gao et al. (2013).

2.3. Effect of Klein-Nishina correction, pair-production and EBL correction

To consistently extend our VHE off-axis afterglow model, we incorporate the effects of correction for Klein-Nishina (KN) scattering cross-section to SSC emission, which becomes relevant when photon energies in the electron's rest frame approach or exceed the electron rest mass energy, $m_e c^2$ (Nakar et al., 2009). In this regime, the energy gain per photon per scattering becomes effectively constant. Following the prescriptions of Nakar et al. (2009) and Mondal et al. (2023), we include the modified Y parameter in the KN regime, denoted as $Y_{\text{KN}} = P_{\text{SSC}}(\gamma)/P_{\text{syn}}(\gamma)$, for both slow ($Y(\gamma_c)$) and fast-cooling ($Y(\gamma_m)$) electron distributions (Nakar et al., 2009; Mondal et al., 2025).

Moreover, we account for the attenuation of TeV photons due to pair production ($\gamma\gamma \rightarrow e^-e^+$) resulting from interactions with low-frequency background photons (optical, UV, and IR), as described by Gould and Schröder (1967). This absorption is modeled through an energy-dependent internal optical depth, $\tau_{\gamma\gamma}(E_\gamma)$, which is used to correct the intrinsic SSC flux at the source (Gould and Schröder, 1967; Joshi and Razzague, 2021). Finally, we further include the attenuation of VHE photons during their propagation through the intergalactic medium due to interactions with the extragalactic background light (EBL), applying the correction factor $\exp[-\tau(E_\gamma, z)]$ following the formalism of Dominguez et al. (2011).

2.4. Effect of Gaussian structure jet on VHE Emission

In a Gaussian structured jet, the angular dependence of both the isotropic-equivalent energy distribution and the bulk Lorentz factor critically determines the production and detectability of VHE emission. Unlike the sharply bounded top-hat jet, the smooth angular profile of a Gaussian jet alleviates the severity of Doppler deboosting for off-axis observers. As a result, the observed flux is less suppressed at larger viewing angles, thereby improving the prospects of detecting significant VHE

emission even for moderately misaligned lines of sight. The visibility of VHE photons is therefore strongly governed by the Doppler boosting factor through the observer viewing angle θ_v . Further, in the process two distinct detection scenarios appear: (i) for $\theta_v < \theta_c$, corresponding to an on-axis geometry, where the observer receives intense emission from the highly relativistic jet core, with the flux peaking at early times due to strong Doppler boosting, (ii) for $\theta_v > \theta_c$, due to dominant Doppler de-boosting, the resulting emission attains lower peak flux and a delayed peak time relative to the on-axis case and (iii) mildly off-axis jet geometry where Gaussian structured jet viewed at a small but non-zero angle. Consequently, the spectral properties are highly sensitive to the ratio θ_v/θ_c . Our recent study (Mondal et al., 2025) shows that a large off-axis viewing angle (exceeding 25°) sharply reduces the probability of detection with CTA, while the VHE detectability is preferred for $\theta_v/\theta_c \leq 2.7$. In the following section, we investigate how these jet intrinsic and extrinsic parameters are correlated in shaping the observed VHE emission from GRB 221009A.

3. Parameter Dependence of VHE Afterglow Emission

Using the described structure jet model, we will study the SSC TeV afterglow features in both the spectral and temporal domains of GRB 221009A. Since both the peak flux and peak time depend sensitively on the underlying afterglow parameters, we perform a comprehensive exploration of the afterglow parameter space by constraining the structured jet properties that favour VHE emission from GRB 221009A. Thus, we systematically examine the spectral and temporal evolution of the afterglow through predicting spectral energy distributions (SEDs) and TeV light curves (LCs).

3.1. Fitting Method

Our structured jet afterglow model is characterized by a parameter set $\Theta_A = E_k, n_0, \eta_c, \theta_{j,\text{max}}, \theta_c, \epsilon_e, \epsilon_B, k, \theta_v$, while the source luminosity distance is at $d_L = 723.6$ Mpc, and $\eta_c = \Gamma_c \beta_c$ is the initial velocity of jet along its core. To fit our Gaussian structured jet model to GeV-TeV data of AGILE GRID and LHAASO, we constrained our afterglow parameter space with seven parameters: $E_k, n_0, \eta_c, \theta_c, \epsilon_e, \epsilon_B, \theta_v$, while keeping $\theta_{j,\text{max}}$ and k fixed to 25° and 2.5 respectively. Here we restrict $\theta_{j,\text{max}}$ value to that value ($\leq 25^\circ$) to avoid errors while performing numerical methods in synchrotron and subsequent SSC flux calculation. To further reduce the number of free parameters, we fix the electron power-law index k to a representative value within the range commonly inferred for GRB afterglows, which is also adopted in the neutrino-flux calculations in later (see section 4.2).

All the data of AGILE GRID and LHAASO is taken from Foffano et al. (2024) and LHAASO Collaboration et al. (2023). We perform posterior parameter inference using the Markov Chain Monte Carlo (MCMC) technique, employing the Python package `emcee`² as the sampler (Foreman-Mackey et al., 2013).

²<https://emcee.readthedocs.io/en/stable/>

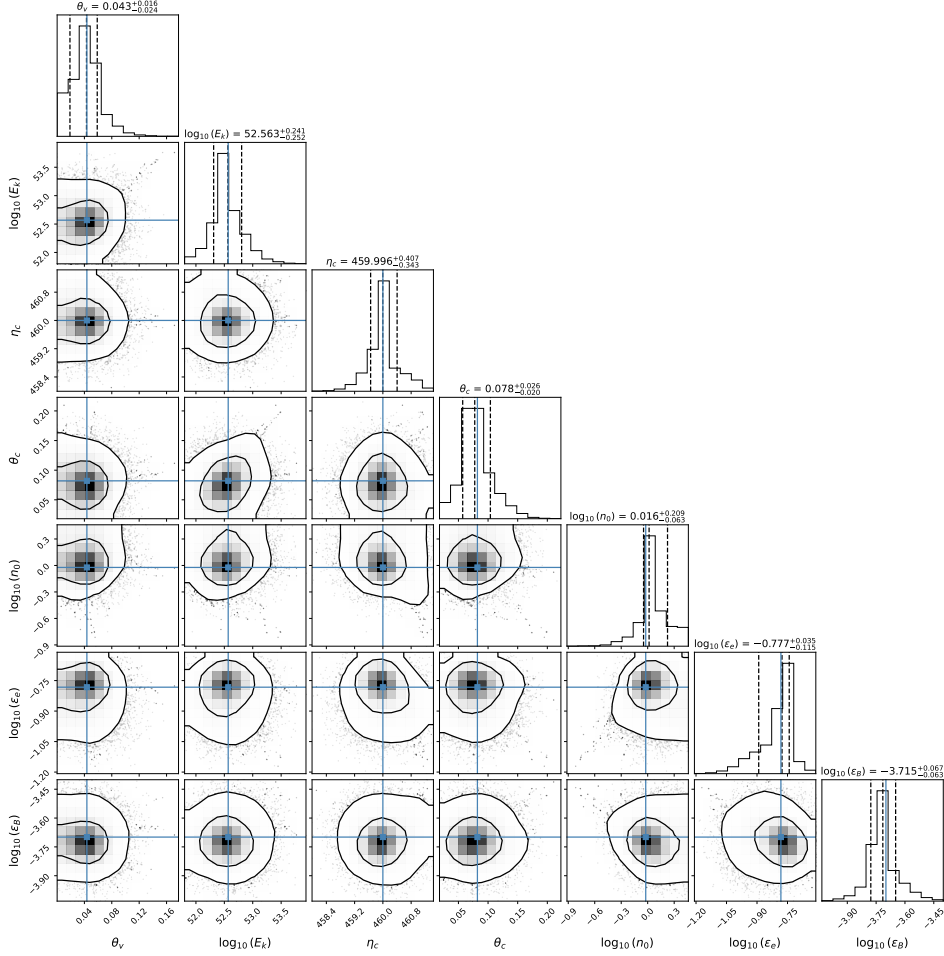


Figure 2: Corner plot showing posterior distributions of afterglow model parameters for GRB 221009A. All the contours enclosing median values and $\pm 1\sigma$ uncertainties. Thin reference lines denote the truth values.

This Bayesian approach enables us to explore the multidimensional parameter space efficiently and estimate posterior probability distributions for the model parameters given the observed GeV–TeV afterglow data. We adopt broad, uniform priors for all free parameters within physically motivated ranges, relevant to GRB afterglow modeling, and do not account for any systematic errors of the instruments. The likelihood function was defined assuming Gaussian uncertainties in the AGILE–GRID and LHAASO flux measurements (Foffano et al., 2024; LHAASO Collaboration et al., 2023).

Initially, to fit the spectra of GRB 221009A, among the three time intervals of the SED (see Section 3.2), the MCMC sampling was performed over the range $T^* + [100, 674]$ s. $T^* = T_0 + 226$ s is the reference time considered in most spectral analyses of GRB 221009A (LHAASO Collaboration et al., 2023; Foffano et al., 2024; Ren et al., 2024b; Abe et al., 2025). The resulting posterior probability densities were obtained using 32 walkers in emcee, each of which was evolved for 2000 iterations to ensure convergence. The parameters of the best-fit model along with their associated confidence intervals ($\pm 1\sigma$) are summarized in Table 1, and the corresponding posterior distributions are illustrated in the corner plot (Figure 2). To extend the analysis to the

Table 1: Best-fit Afterglow model parameters from simultaneous interpretation of VHE light curves and SED spectrum of GRB 221009A. Uncertainties denote 1σ credible ranges from MCMC posterior distributions.

Parameter	Range
$\log E_k$ (erg)	$52.66^{+0.24}_{-0.25}$
$\log n_0$ (cm $^{-3}$)	$0.02^{+0.21}_{-0.06}$
η_c	$459.56^{+0.41}_{-0.34}$
$\log \epsilon_e$	$-0.78^{+0.04}_{-0.12}$
$\log \epsilon_B$	$-3.71^{+0.07}_{-0.06}$
θ_v (deg)	$2.46^{+0.92}_{-1.37}$ °
θ_c (deg)	$4.41^{+1.49}_{-1.14}$ °

other two SED intervals, we allow the fractional magnetic field energy ϵ_B , which represents the fraction of post-shock energy transferred in magnetic fields, to evolve as a function of observer time under adiabatic expansion in the ISM, while keeping all other parameters within their $\pm 1\sigma$ credible intervals. This time-dependent treatment yields a consistent fit to the broad-

band SEDs and provides good agreement with the GeV–TeV light-curve data of GRB 221009A observed by LHAASO and AGILE–GRID.

3.2. VHE Spectral modelling of GRB 221009A

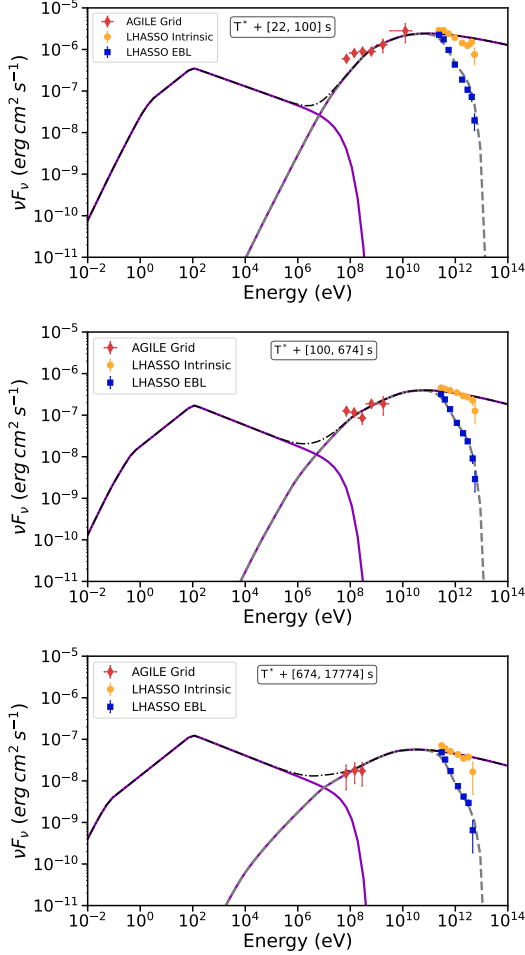


Figure 3: Broadband SEDs of GRB 221009A at three time intervals derived from the structured-jet afterglow model. Top: $T^* + [22, 100]$ s; middle: $T^* + [100, 674]$ s; bottom: $T^* + [674, 17774]$ s, where $T^* = T_0 + 226$ s. Red diamonds denote AGILE–GRID GeV data, orange circles show LHAASO intrinsic TeV fluxes, and blue squares include EBL attenuation. The solid purple curves represent the intrinsic model spectra, with the low-energy hump from synchrotron emission and the high-energy hump from SSC radiation. The dashed grey lines show spectra corrected for EBL attenuation, while dash-dotted black lines indicate the total synchrotron + SSC emission.

In this section, we validate our structured jet model by globally fitting the early afterglow GeV–TeV spectral data of GRB 221009A from AGILE and LHAASO. As AGILE GRID GeV data are not available for the very early afterglow phase of the GRB, specifically $T^* + [5, 14]$ s and $T^* + [14, 22]$ s. In our analysis, we have mainly used the GeV and TeV spectral data of the time bin of $T_1 = T^* + [22, 100]$ s, $T_2 = T^* + [100, 674]$ s and $T_3 = T^* + [674, 17774]$ s (Foffano et al., 2024). Figure 3 represents the optimized synchrotron and SSC spectra of GRB 221009A for these three distinct time intervals. The spectra incorporate the Klein-Nishina effect, corrections due to $\gamma\gamma$ -pair

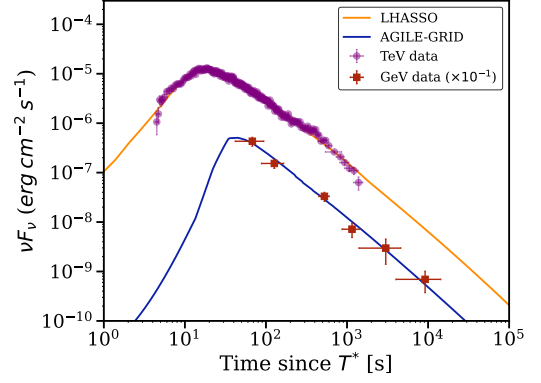


Figure 4: Afterglow light curves of GRB 221009A in the GeV and TeV bands modeled with the Gaussian structured-jet framework. The orange curve represents the TeV LC, fitted with LHAASO TeV data for 0.3–5 TeV, and the blue curve shows the GeV LC fit to AGILE–GRID GeV data of 50 MeV–3 GeV. Purple circles correspond to the observed LHAASO TeV data, while dark-red squares denote AGILE–GRID GeV data (scaled by $\times 10^{-1}$).

production optical depth, and the EBL attenuation of TeV photons.

SEDs of all of these time intervals collectively comprise the rising, peaking, and decaying phases of the afterglow. In these SED panels, all the first spectral humps, rising from low energy, ranging from $\sim 10^{-2}$ eV up to $\lesssim 1$ GeV, are dominated by synchrotron emission, while the second humps correspond to SSC radiation. Solid lines represent intrinsic model spectra, dashed lines show the EBL attenuated spectra and $\gamma\gamma$ annihilation corrected spectra, and dashed-dot lines depict the combined synchrotron and SSC components. In particular, the afterglow flux begins to be dominated by the SSC around 1 GeV, and significant EBL attenuation becomes apparent above ~ 10 TeV.

Our model fits the observed data at the jet observer viewing angle $\theta_v \geq 0.6^\circ$, and the spectra lie in the regime of $\theta_c > \theta_v$ at all intervals. These parameter values lead to a mildly off-axis jet scenario, enhancing the SSC flux due to Doppler boosting. This result is in good agreement with the structured-jet interpretation proposed by O’Connor et al. (2023). Furthermore, we found that all of the spectra are well explained in $\epsilon_e \gg \epsilon_B$, indicating that inverse Compton cooling dominates over magnetic energy losses, thereby amplifying the SSC component. The best-fit spectral parameters derived from this analysis are subsequently employed to calculate the corresponding neutrino flux in section 4. To further associate this energy with the neutrino flux calculation, we need to estimate the isotropic jet kinetic energy $E_{k,iso}$ along a given direction of observer viewing angle θ_v . The detailed calculation is discussed in Section 4.3.

3.3. TeV afterglow Light Curve

Figure 4 presents the afterglow light curve of GRB 221009A, which is obtained through our model by fitting GeV and TeV gamma-ray data from AGILE GRID and LHAASO, respectively. The TeV light curve of GRB 221009A is estimated in the energy range of 0.3 – 5TeV, while the GeV one is calculated in the range of 50MeV – 3GeV. The Light curves are fitted using the afterglow parameters listed in Table 1. Here, the VHE photons

are minimally Doppler de-boosted through a mildly off-axis viewing geometry.

The light curve exhibits a two-phase structure, characterized by a gradual rise to the peak followed by a steep decay. The observed TeV light curves include KN corrections (Nakar et al., 2009; Mondal et al., 2025), pair-production optical depth (Joshi and Razzaque, 2021) and an account for attenuation due to extragalactic background light (EBL) (Dominguez et al., 2011). We find that a higher kinetic energy (E_k), ambient density (n_0), and bulk Lorentz factor at the jet's core (Γ_c) strongly influence the observed SSC flux by increasing the seed photon population for inverse Compton scattering. For both GeV-TeV cases, a mildly off-axis structured jet scenario allows the observer to receive intense, early-time emission from the jet core due to its moderately high Lorentz factor. Furthermore, these GeV-TeV light curves also follow $\epsilon_e > \epsilon_B$, which is crucial for efficient SSC production in the forward shock afterglow model. Note that a feature around 600 s in the TeV light curve was previously interpreted as a jet break by LHAASO Collaboration et al. (2023). However, the GeV light curve in Figure 4 does not show such a break. Therefore, we do not assume a jet break during $T \lesssim 10^4$ s in our analysis. This is consistent with conclusions drawn by (Geng et al., 2025; Kusafuka and Asano, 2025; Barnard et al., 2025).

4. Neutrino production during Afterglow Phase

In this work, we focus on the ISM case, where the adiabatic forward shock is considered one of the most promising sites for ultra-high-energy cosmic-ray (UHECR) acceleration and the subsequent production of high-energy neutrinos in the PeV–EeV range. In our analysis, we compute the neutrino spectrum arising from photo-hadronic ($p\gamma$) interactions between accelerated protons and target photons within the shocked region. Our present calculation accounts only for neutrinos produced via these $p\gamma$ interactions, while the secondary electrons and γ -rays generated in these processes have not yet been followed through their cascade development. Incorporating these secondary cascades would provide a more comprehensive picture of the multi messenger emission and represents an important direction for future work.

4.1. Neutrino flux calculation from $p\gamma$ interaction channel

Nonthermal protons interacting with seed photons produce pions through photo-hadronic processes, which subsequently decay into secondary particles and neutrinos. Neutral pions decay into two γ -ray photons, while charged pions decay predominantly into a muon and a muon neutrino (or antineutrino) ($p\gamma \rightarrow \pi^\pm \rightarrow \mu^\pm + \nu_\mu(\bar{\nu}_\mu)$). The resulting positively (negatively) charged muons undergo a three-body decay and yield electrons (positrons) together with neutrinos (electron and muon types): ($\mu^\pm \rightarrow e^\pm + \nu_e(\bar{\nu}_e) + \nu_\mu(\bar{\nu}_\mu)$). This decay chain generates an initial flavor ratio of $\nu_e : \nu_\mu : \nu_\tau \sim (1 : 2 : 0)$ at the source, while this ratio changes to $\nu_e : \nu_\mu : \nu_\tau \sim (1 : 1 : 1)$ at Earth after oscillation, which is independent of the neutrino energy.

In this work, we calculate the neutrino flux for the three neutrino flavors ν_μ , ν_e , and ν_τ at Earth, taking into account the effects of the neutrino oscillations. We estimate neutrino fluxes associated with both on-axis and off-axis Gaussian structured jets from a GRB event at a cosmological redshift of $z = 0.151$ under an extreme energetic scenario. In addition, we derive the time-integrated upper limit sensitivity curves for this point-like source based on the planned next-generation high-energy neutrino detectors, IceCube Gen2 and GRAND200k. Further using our best-fit model parameters from the VHE γ -ray leptonic model (section 3.1), we compute the neutrino flux for GRB 221009A. Later, we explore how correlations among model parameters govern the neutrino flux, and also how their extreme combination leads the number of muon neutrino events towards the 90% confidence upper limit (Gehrels, 1986) of detection for next-generation neutrino detectors.

4.2. Neutrino flux from pion and muon decay channel

To calculate the neutrino flux arising from the photo-meson decay channel in GRBs, we consider the $p\gamma$ interaction formalisms of Razzaque (2013), where nonthermal protons accelerated in the external forward shock following a power law spectrum $dN/dE_p \propto E_p^{-2}$ and interacting with target synchrotron photons in an adiabatic interstellar medium. Here, E_p is the proton energy, and later we used E_π and E_ν , which are the pion energy and energy of neutrino, respectively. The resulting neutrino flux observed at Earth depends on several factors — the photon number density $n(E_\gamma)$, the photo-pion production optical depth $\tau_{p\gamma}(E_p)$, and the cosmic-ray proton flux $\phi_p(E_p)$ (Razzaque, 2013). The charged pion flux $\phi_\pi(E_\pi)$ is determined from the interaction optical depth $\tau_{p\gamma}(E_p)$ and proton flux $\phi_p(E_p)$, from which the subsequent decay chains yield muons and neutrinos.

The muon neutrino flux at the Earth $\phi_{\nu_\mu}(E_\nu)$ from pion decay, and electron neutrino and muon anti-neutrino flux $\phi_{\nu_e}(E_\nu)$, and $\phi_{\bar{\nu}_\mu}(E_\nu)$ from muon decay are calculated from Razzaque (2013) using standard convolution integrals involving appropriate decay scaling functions therein. These preliminary flux calculations do not include neutrino oscillations. However, these calculations typically adopt energy fraction mappings such as $E_\nu \approx 0.2 E_p$ for the pion channel, reflecting the typical partitioning of energy between the parent proton and the resulting neutrinos (Razzaque, 2013; Adriani et al., 2025). Now, to estimate the neutrino flux at Earth after taking into account neutrino oscillation over the astrophysical distance, there should be three flux components: $\nu_e + \bar{\nu}_e$, $\nu_\mu + \bar{\nu}_\mu$ and $\nu_\tau + \bar{\nu}_\tau$. Using the contribution from neutrino flavor mixing parameters due to neutrino oscillations over astrophysical distance, we further calculated neutrino fluxes of all three flavors — $\phi_{\nu_e + \bar{\nu}_e}^\oplus$, $\phi_{\nu_\mu + \bar{\nu}_\mu}^\oplus$, and $\phi_{\nu_\tau + \bar{\nu}_\tau}^\oplus$. For any $\nu + \bar{\nu}$ flavor, $\phi_{\nu + \bar{\nu}}^\oplus$ is the neutrino flux at Earth after oscillations.

All these neutrino fluxes of all three flavors are primarily detected by a set of parameters that strongly govern the $p\gamma$ hadronic channel for neutrino emission. These parameters are— isotropic-equivalent kinetic energy ($E_{k,iso}$), number density of the circumburst (n_0), initial bulk Lorentz factor ($\Gamma_0 \equiv \eta_c$), the

fraction energy transferred to electron (ϵ_e), the magnetic field fraction (ϵ_B), fraction of kinetic energy imparted to non-thermal protons (ϵ_p), and electron power-law index (k). Based on this parameter space, we will now explore how the neutrino flux varies and how their correlation leads to estimating the neutrino events at the 90% C.L.

4.3. Effect of structured-jet parameters on neutrino flux

One of the key structured-jet parameters that governs the estimation of high-energy neutrino flux is the isotropic-equivalent kinetic energy, $E_{k,iso}$, of the blast wave. In our off-axis Gaussian structured-jet model, the angular distribution of jet energy is described by $\varepsilon(\theta)$, which is characterized by the jet kinetic energy per unit solid angle ε_c . This ε_c is obtained from the jet total kinetic energy E_k , which is calculated by integrating the distribution of angular energy profile over the total solid angle $d\Omega$ within the jet surface in between $0 \leq \theta \leq \theta_{j,max}$ as following,

$$E_k = 2\pi \int_0^{\theta_{j,max}} \varepsilon(\theta) \sin \theta d\theta. \quad (5)$$

For small jet opening angles ($\sin \theta \approx \theta$), this simplifies to

$$E_k = 2\pi \varepsilon_c \int_0^{\theta_{j,max}} \theta \exp\left(-\frac{\theta^2}{2\theta_c^2}\right) d\theta, \quad (6)$$

The integration yields the normalized energy distribution, and jet kinetic energy per unit solid angle at the core ε_c can be expressed in terms of the total jet energy E_k as

$$\varepsilon_c \approx \frac{E_k}{\pi\theta_c^2 \left(1 - e^{-\theta_{j,max}^2/\theta_c^2}\right)}. \quad (7)$$

The isotropic-equivalent kinetic energy $E_{k,iso}$ perceived by an observer located at a viewing angle θ_v depends on the angular energy profile of the jet. Instead of assuming a single line-of-sight value, we compute the effective kinetic energy within a narrow cone of angular width $\Delta\theta$ centred on θ_v , such that

$$E_k(\theta_v) = 2\pi \varepsilon_c \int_{\theta_v-\Delta\theta}^{\theta_v+\Delta\theta} \theta \exp\left(-\frac{\theta^2}{2\theta_c^2}\right) d\theta, \quad (8)$$

where $\Delta\theta \approx 1/\Gamma(\theta_v, t)$ specifies the angular width of the region effectively visible to the observer at time $t > t_{dec}$ due to relativistic beaming. This formulation presents a more feasible scenario in which the structured jet emission contributes to the observed flux and, consequently, to neutrino production.

The isotropic-equivalent kinetic energy along the observer's line of sight is then given by

$$E_{k,iso}(\theta_v) = 4\pi \bar{\varepsilon}(\theta_v), \quad (9)$$

where the effective energy per unit solid angle is

$$\bar{\varepsilon}(\theta_v) = \varepsilon_c \exp\left(-\frac{\theta_v^2}{2\theta_c^2}\right). \quad (10)$$

This approach effectively connects the angular energy structure of the jet with the observer's geometry, enabling the estimation of $E_{k,iso}$ that directly influences the predicted high-energy neutrino flux. Due to the dependency on jet geometry, the angular profile of jet velocity also becomes $\Gamma_0(\theta_v)\beta_0(\theta_v)$. The derived $E_{k,iso}(\theta_v)$ is subsequently used in our photo-hadronic ($p\gamma$) interaction framework for further calculations, to study parameter-space correlations and to estimate neutrino event numbers for a given neutrino detector.

4.4. Results

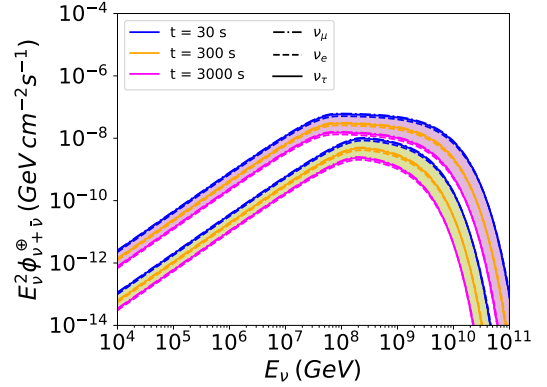


Figure 5: Neutrino flux for a GRB at $z = 0.151$ in two viewing geometries. The upper (purple) band corresponds to the on-axis case ($\theta_v < \theta_c$; here $\theta_c = 6^\circ$, $\theta_v = 3^\circ$), while the lower (yellow) band shows the mildly off-axis case ($\theta_v > \theta_c$; $\theta_v = 13^\circ$). Within each band, all three neutrino flavor fluxes at Earth after oscillation are plotted for the three observer time epochs $t > t_{dec} \in \{30, 300, 3000\}$ s: $\nu_\mu + \bar{\nu}_\mu$ (dash-dotted curve), $\nu_e + \bar{\nu}_e$ (dashed curve), and $\nu_\tau + \bar{\nu}_\tau$ (solid curve). Model parameters: $E_k = 3.1 \times 10^{53}$ erg (implying $E_{k,iso}^{on} \sim 1 \times 10^{56}$ erg and $E_{k,iso}^{off} \sim 1 \times 10^{55}$ erg), $\epsilon_e = \epsilon_B = 0.1$, $\epsilon_p = 1.0$, $k = 2.5$.

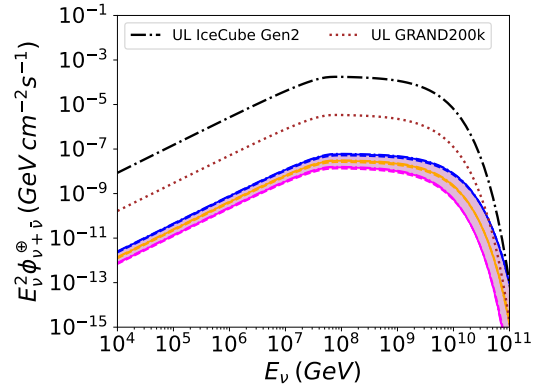


Figure 6: Time-integrated 90% upper limit sensitivity curve of neutrino spectrum is plotted for ν_μ events at $z = 0.151$, for the detector geometry of IceCube Gen2 (dash-dotted curve) and GRAND200k (dotted curve). The purple band shows the on-axis neutrino flux from Figure 5.

Figure 5 presents the neutrino flux, $E_\nu^2 \phi_{\nu+\bar{\nu}}^\oplus$, observed at Earth after neutrino oscillation taken into account for a simulated GRB event located at redshift $z = 0.151$. This figure compares two geometrical scenarios: (a) the on-axis case ($\theta_v < \theta_c$) – upper purple band and (b) the mildly off-axis case ($\theta_v > \theta_c$) – lower

yellow band, with the jet core angle fixed at $\theta_c = 6^\circ$, and the viewing angle set to $\theta_v = 3^\circ$ for the on-axis and $\theta_v = 13^\circ$ for the mildly off-axis scenario. Blue, orange, and magenta curves represent neutrino flux estimated at successive time epochs at $t > t_{dec} \in 30s, 300s, 3000s$, respectively, illustrating the temporal decline in flux and t_{dec} is the deceleration time scale (Razzaque, 2013). The upper purple band corresponds to the on-axis neutrino spectrum, displaying the summed fluxes of $\nu_\mu + \bar{\nu}_\mu$ (dash-dotted), $\nu_e + \bar{\nu}_e$ (dashed), and $\nu_\tau + \bar{\nu}_\tau$ (solid), with neutrino oscillation effects included. The lower yellow band shows the corresponding off-axis neutrino spectra for the same neutrino flavor eigenstates and time epochs. The on-axis flux is higher than the off-axis scenario, reflecting enhanced Doppler boosting and a brighter photon target field for $\theta_v < \theta_c$, which increases the overall neutrino production. In comparison, for off-axis geometries, the neutrino flux is suppressed due to the off-axis angular structure of the jet and the effects of Doppler deboosting, which collectively reduce the flux observed at Earth.

As individual GRBs are effectively point sources for high-energy neutrino telescopes, it is essential to estimate the upper limit sensitivity for such sources, as this value can vary depending on the detector's geometry specification. To evaluate these limits, we utilize the effective areas of IceCube-Gen2³ and GRAND200k (Álvarez-Muñiz et al., 2020). The number of detected neutrino events for a single neutrino flavor over a finite time window and energy range from a given GRB by a specific neutrino detector has been calculated as —

$$N_{\text{evt}} = \int_{T_1}^{T_2} \int_{E_1}^{E_2} \phi_{\nu+\bar{\nu}}^{\oplus} A_{\text{eff}}(E) dE dt, \quad (11)$$

where $\phi_{\nu+\bar{\nu}}^{\oplus} = d^2N/(dE dt)$ is the differential neutrino flux at Earth and $A_{\text{eff}}(E)$ is the effective area of a specific neutrino detector for the relevant neutrino flavor.

For estimating the flux upper limit, we adopt the 90% C.L. Poisson upper bound on the number of events, $N_{\text{evt}}^{90} = 3.890$ (Gehrels, 1986). For a chosen interval $[30, 3000]$ s and given the effective area of IceCube Gen2 and GRAND200k, we first calculate the number of muon neutrino events within the specified energy and time window using equation 11. The normalization factor ϕ_0 is then defined as the ratio of N_{evt}^{90} to the estimated total number of muon neutrino events for that interval. Finally, the product $\phi_0 E_\nu^2 \phi_\nu^{\oplus}(E)$ gives the corresponding 90% C.L. upper limit (UL) sensitivity curve for a point-like source, consistently constraining the flux. The purple band of Figure 6 shows the on-axis neutrino flux from Figure 5. The resulting time-integrated upper limit curve (90% C.L) in Figure 6 is calculated for ν_μ events at $z = 0.151$, for the detector geometry of IceCube Gen2 (dash-dotted curve) and GRAND200k (dotted curve).

Now, instead of a simulated GRB event (Figures 5 and 6), we illustrate the neutrino flux of GRB 221009A at redshift $z = 0.151$ in Figure 7. As discussed above, neutrino spectra are decomposed into the three neutrino flavors ν_μ , ν_e , and ν_τ , evaluated over successive time intervals $T_1 = T^* + [22, 100]$ s,

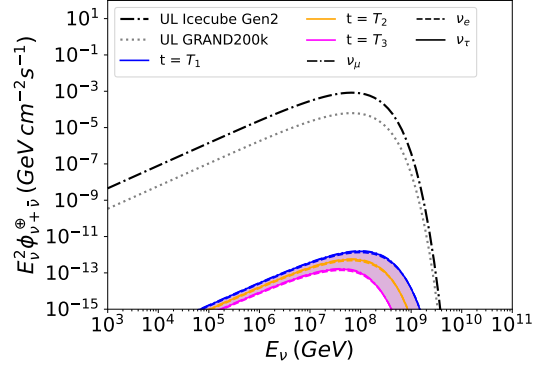


Figure 7: Neutrino Flux of GRB 221009A at three time intervals T_1 , T_2 and T_3 . Black Dashed-dot and grey dotted line are the upper limit sensitivity curve obtained for IceCube Gen2 and GRAND 200k for the time interval T_2 .

$T_2 = T^* + [100, 674]$ s, and $T_3 = T^* + [674, 1774]$ s respectively. The shaded purple band corresponds to the mildly off-axis neutrino emission scenario, comprising the combined fluxes of $\nu_\mu + \bar{\nu}_\mu$ (dashed-dotted), $\nu_e + \bar{\nu}_e$ (dashed), and $\nu_\tau + \bar{\nu}_\tau$ (solid). Here, the neutrino spectra, similar to blue, orange, and magenta in Figure 5, denote the temporal evolution of the flux across these three time intervals. These fluxes are obtained using the same afterglow parameters that reproduce the observed GeV–TeV emission of GRB 221009A, within a blast wave framework expanding in a constant density ISM and evolving adiabatically. All spectra include flavor mixing due to neutrino oscillations during propagation to Earth. The peak flux systematically decreases with time as the external shock decelerates. We further estimated the upper limit sensitivity curve at interval T_2 for ν_μ events. We can see the predicted fluxes for all three flavors remain well below the upper limit sensitivity limits of IceCube Gen2 (dashed-dot) and GRAND200k (dashed). This result confirms the expected absence of neutrino detections from GRB 221009A with our Gaussian structured-jet afterglow model.

5. Constraints from Afterglow Neutrino Emission

In the preceding sections, we have calculated neutrino fluxes from GRB point sources and evaluated time-integrated upper limit sensitivities using the effective areas of IceCube Gen2 and GRAND200k. These results showcase that, for GRB 221009A, the expected upper limit sensitivity for ν_μ events is substantially higher for GRAND200k compared to IceCube Gen2, driven by GRAND200k's comparatively larger effective area (see Figure 7). The number of detectable muon neutrino events is further determined by the differential flux at Earth, $\phi_{\nu_\mu}^{\oplus}(E_\nu)$, which depends directly on the parameters of the underlying hadronic model.

Our analysis (subsection 4.4) demonstrates that both the predicted neutrino flux and its corresponding sensitivity limits are strongly influenced by key hadronic model parameters, as highlighted in Figures 6 and 7. Robust constraints in the feasible parameter space necessitate a systematic exploration of their

³<https://icecube-gen2.wisc.edu/science/publications/tdr/>

correlations across a wide energy range (GeV–PeV) and temporal scales. Such comprehensive multidimensional studies are essential to identify the regions where neutrino event detections maximize and to establish realistic detection expectations for future experiments at the 90% C.L. searches.

5.1. Correlations among the model parameters

To analyze how key hadronic model parameters affect neutrino flux and event rates, we systematically examine their correlations over broad energy and timescale ranges by estimating muon neutrino events using the geometry of the GRAND200k detector, which offers a slightly larger effective area than IceCube Gen2.

To explore the parameter space favorable to a detectable muon neutrino event, we perform simulations for those events by systematically varying the key model parameters over broad ranges motivated by afterglow modeling in the literature. We consider a simulated GRB event at a fixed cosmological redshift $z \sim 0.151$. We further fix the initial bulk Lorentz factor of the jet $\Gamma_0 = 460$ and $k = 2.5$. The other model parameters are sampled from logarithmic uniform distributions spanning optimistic intervals.

$$\begin{aligned} E_{k,\text{iso}} &\in [10^{53}, 10^{56}] \text{ erg}, \\ n_0 &\in [0.3, 30] \text{ cm}^{-3}, \\ \epsilon_e &\in [0.01, 0.3], \\ \epsilon_B &\in [10^{-4}, 10^{-1}], \\ \epsilon_p &\in [10^{-2}, 10^0], \end{aligned}$$

To investigate which parameter combinations most strongly drive detectability, we generate two-dimensional contour maps for every pair among $(E_{k,\text{iso}}, n_0, \epsilon_e, \epsilon_B, \epsilon_p)$, with the color scale showcasing the number of muon neutrino events (see Figures 8, 9, 10). In all panels, lighter shades correspond to larger muon neutrino events (N_μ). The color maps show a clear trend, increasing $E_{k,\text{iso}}, n_0, \epsilon_e, \epsilon_B,$ or ϵ_p raises the predicted N_μ .

Physically, this reflects the fact that a more energetic blast wave ($E_{k,\text{iso}} \gtrsim 10^{55}$ erg) interacting with a denser circumburst medium ($n_0 \gtrsim 1 \text{ cm}^{-3}$) produces a larger population of shock-accelerated protons and photons, thereby boosting the efficiency of $p\gamma$ interactions. Along with a higher fraction of energy imparted to relativistic electrons ($\epsilon_e \gtrsim 1 \times 10^{-1}$), it brightens the target photon density, and leads to a larger photopion efficiency, resulting in more neutrinos. Larger magnetic fraction ($\epsilon_B \gtrsim 1 \times 10^{-3}$) further amplifies the target photon density and synchrotron cooling, which serves as the target field for neutrino production. A relatively larger proton fraction ($\epsilon_p \gtrsim 1 \times 10^{-1}$) directly boosts the non-thermal proton power available for $p\gamma$ interactions. The influence of Γ_0 is comparatively weak relative to the other parameters, so we keep it fixed.

For clarity, Figure 8 presents $E_{k,\text{iso}}$ scanned against $n_0, \epsilon_e, \epsilon_B,$ and ϵ_p ; Figure 9 shows n_0 versus $\epsilon_e, \epsilon_B,$ and ϵ_p ; and Figure 10 displays the microphysical variation between $(\epsilon_e, \epsilon_B), (\epsilon_e, \epsilon_p),$ and (ϵ_B, ϵ_p) . In each panel, parameters not shown on the axes are held fixed at the optimistic values mentioned in the captions (e.g., when varying $E_{k,\text{iso}}$ with n_0 , we set $\epsilon_e = 0.1, \epsilon_B = 0.1,$ and $\epsilon_p = 1.0$; when varying $E_{k,\text{iso}}$ with ϵ_e , we set

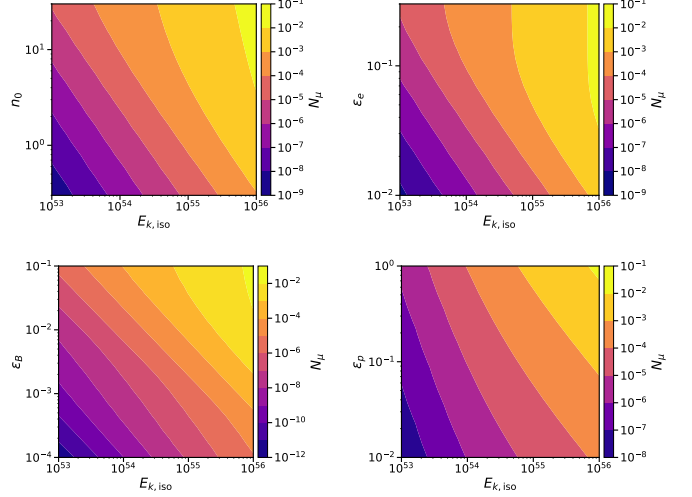


Figure 8: Number of muon neutrino events N_μ for GRAND200k over $t \in \{20, 2000\}$ s as a function of $E_{k,\text{iso}}$ and, panelwise, n_0 (top-left), ϵ_e (top-right), ϵ_B (bottom-left), and ϵ_p (bottom-right). Across all panels, N_μ increases monotonically with both $E_{k,\text{iso}}$ and the corresponding model parameter. Within the scanned ranges, $N_\mu < 1$, consistent with non-detection. Throughout these panels, when varying $E_{k,\text{iso}}$ with a given parameter, the remaining parameters are held fixed at $\epsilon_e = 0.1, \epsilon_B = 0.1, \epsilon_p = 1.0,$ and $n_0 = 10$.

$n_0 = 10, \epsilon_B = 0.1,$ and $\epsilon_p = 1.0$). Thus, these contour mappings reflect the parameter combinations that can yield comparable N_μ and identify the regimes most favorable for GRAND200k detectability.

6. Summary and Conclusions

In this work, we modeled the very high energy afterglow of GRB 221009A with an external forward shock from a Gaussian structured jet expanding into a uniform ISM medium, and we computed the accompanying, $p\gamma$ neutrino emission in the PeV–EeV range.

In section 3, we applied our Gaussian structured jet model to reproduce the GeV–TeV afterglow observed by AGILE-GRID and LHAASO to study the SSC-driven VHE afterglow features in both the spectral (SEDs Figure 3) and temporal (LCs Figure 4) domains of GRB 221009A. We validated the model through detailed spectral fits of the GeV–TeV afterglow across three early-time intervals, accounting for KN effects, the opacity of internal $\gamma\gamma$ pair production, and EBL attenuation. We observe the resulting best-fit afterglow parameters from MCMC sampling favor a mildly off-axis jet structure. The resulting viewing angle $\theta_v = 2.46^\circ$, and jet core angle $\theta_c = 4.41^\circ$ drives the $E_{k,\text{iso}} \sim 2 \times 10^{55}$ erg and here n_0 is 0.97 cm^{-3} respectively. In both SEDs and LCs, the fits require $\epsilon_e \gg \epsilon_B$, which makes SSC emission strongly dominates at VHE. To produce a consistent fit in the SEDs, we consider a time-dependent magnetic energy fraction across distinct time intervals. Slightly lower value of jet core angle $\theta_c \sim 3^\circ$ has been proposed by Zheng et al. (2024).

The SEDs in Figure 3 display both synchrotron and SSC hump, with SSC dominating beyond (~ 1) GeV and strong suppression of EBL above (~ 10) TeV. Figure 4 depicts the light

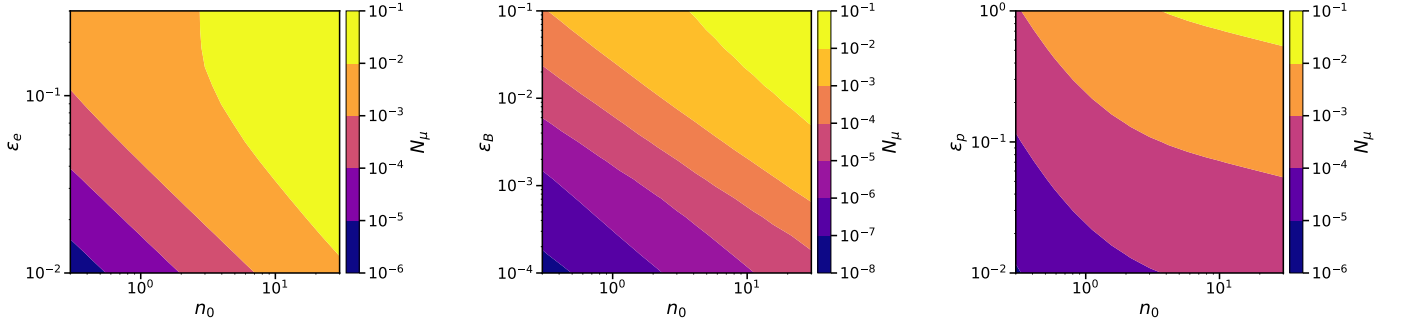


Figure 9: Contour maps of the predicted event yield N_μ for GRAND200k over $t \in \{20, 2000\}$ s, shown in the n_0 - ϵ_e (left), n_0 - ϵ_B (middle), and n_0 - ϵ_p (right) planes. While varying one parameter with n_0 , others fixed at $\epsilon_e = 0.1$, $\epsilon_B = 0.1$, $\epsilon_p = 1.0$, and $E_{k,iso} = 10^{56}$ erg accordingly. The yield grows with both n_0 and the associated microphysical parameter, with the strongest sensitivity along the n_0 - ϵ_p direction.

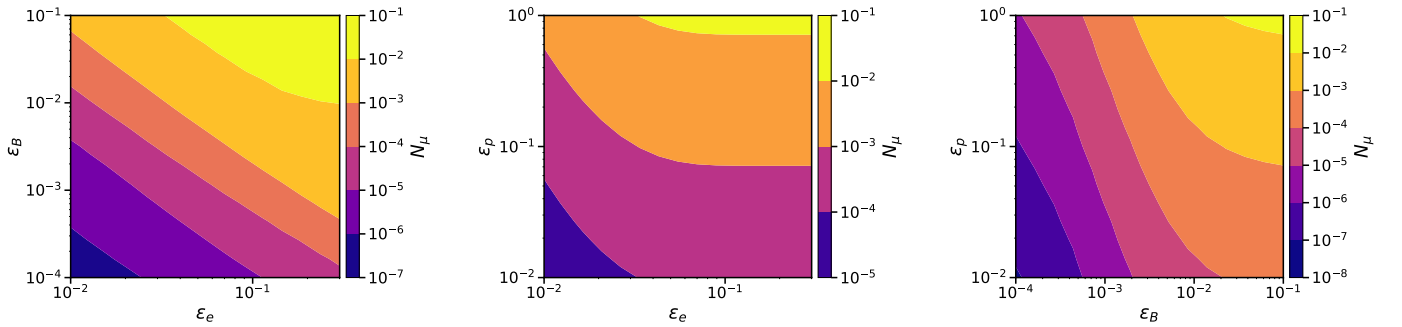


Figure 10: Variation in the predicted GRAND200k event yield (N_μ) as a function of microphysical parameter pairs—(ϵ_e , ϵ_B) (left), (ϵ_e , ϵ_p) (center), and (ϵ_B , ϵ_p) (right), with other parameters fixed at $\epsilon_e = 0.1$, $\epsilon_B = 0.1$, $\epsilon_p = 1.0$, $n_0 = 10$ and $E_{k,iso} = 10^{56}$ erg accordingly. The contour maps show that increasing either parameter in a pair amplifies the expected neutrino event rate, with particularly strong sensitivity for joint increases in ϵ_e and ϵ_p or ϵ_B and ϵ_p , underscoring the importance of electron and proton acceleration efficiencies for neutrino production.

curve that explains the AGILE GRID GeV data (50 MeV–3 GeV) and LHAASO TeV data (0.3–5 TeV). Our findings are consistent with independent structured-jet studies of GRB 221009A by O’Connor et al. (2023); Gill and Granot (2023). However, O’Connor et al. (2023) primarily explains X-ray and OIR light curves and late time afterglow data with a shallow power law structured jet model, where the afterglow best-fit parameters are consistent with our results. Also Gill and Granot (2023), explain X-ray and optical light curves of GRB 221009A with a forward shock structured jet model in a wind medium and Ren et al. (2024b) also, fit the multi-wavelength data of GRB 221009A with a structured jet geometry, taking a transition from ISM to wind-driven medium. For both cases, $E_{k,iso}$ is comparable to our case.

In section 4, we calculate the neutrino on-axis and off-axis flux of the $p\gamma$ interaction channel. Our neutrino flux has been calculated considering the neutrino oscillation effect at Earth at time $t > t_{dec}$, and comprises three neutrino flavors ν_μ , ν_e and ν_τ (see Figure 5). Considering the effective areas of IceCube Gen2 and GRAND200k, we obtain neutrino event counts over a given time scale and propose a formalism to estimate the time-integrated upper limit sensitivity curve for point-like sources. A comparison of viewing geometries in Figure 5, for a simulated GRB event at $z = 0.151$, reveals that the on-axis geometry of the jet yields higher neutrino fluxes than the off-axis ones,

due to stronger Doppler boosting and larger target photon densities. Nevertheless, even optimistic on-axis scenarios showcase in Figure 6 that the neutrino flux remains below the single-burst upper limit sensitivity curve. Furthermore, we estimated the neutrino flux upper limit curve of GRB 221009A (see Figure 7) using the effective areas of IceCube Gen2 and GRAND200k for the time interval $T_2 = T^* + [100, 674]$ s for muon neutrino events. The same afterglow parameters given in section 3 are considered for neutrino flux calculations. In the Figure 7, we observe that the neutrino fluxes for all three flavors remain well below the upper limit sensitivity limits of IceCube Gen2 and GRAND200k.

Finally, in Section 5, we investigate how hadronic model parameters impact neutrino flux and event rates. For this purpose, we examine the model parameter correlations simulating GRB events by estimating muon neutrino events over broad energy and timescale ranges using the geometry of the GRAND200k detector. The GRAND200k detector is considered over IceCube Gen2 in this correlation study as it offers a slightly larger effective area. During the simulation, we keep $z \sim 0.151$, initial bulk Lorentz factor of the jet $\Gamma_0 = 460$ and electron spectral index $k = 2.5$ fixed. Other model parameters are sampled from logarithmic uniform distributions spanning optimistic intervals. We find that a more energetic blast wave, interacting with a denser circumburst medium, produces a larger N_μ events. Further, a

higher fraction of ϵ_e , ϵ_B and ϵ_p enhances the neutrino production, which is shown in our Figure 8, 9, and 10. However, the effect of Γ_0 is not as pronounced compared to other parameters, hence we have kept it fixed.

Our study highlights the significance of jet angular structure, particularly the on-axis and off-axis geometry, in shaping both the electromagnetic and neutrino afterglow signatures of GRBs. Furthermore, our exploration of parameter space reveals the paths forward for enhancing joint VHE and neutrino detections in future observatories, providing clear criteria for the necessary conditions for detectability. While GRBs remain viable candidates for ultra-high-energy cosmic ray sources, our results suggest that only particularly energetic, nearby, and efficiently baryon-loaded bursts are likely to produce detectable neutrino and cosmic-ray signals, thereby refining the search for the most promising multi messenger events.

Acknowledgements

TM acknowledge the financial support received through the Prime Minister’s Research Fellowship (PMRF). TM expresses sincere gratitude to the Centre for Astro-Particle Physics (CAPP) and the Department of Physics at the University of Johannesburg, funded by a BRICS STI grant to SR, where part of this work was completed. TM is grateful to Prof. Resmi Lekshmi (IIST, Trivandrum) for her valuable guidance and continuous support throughout this work. TM also acknowledge the use of the Paramshakti Supercomputing Facility at IIT Kharagpur, established under the National Supercomputing Mission, Government of India, for providing the high-performance computational resources essential to this work. The authors also thank Prof. Sarira Sahu for helpful discussions and are also thankful to Sabyasachi Chakraborty (IIT Kharagpur) and Ajay Sharma (S.N. Bose National Centre for Basic Sciences) for further valuable discussions.

References

- Aartsen, M., Ackermann, M., Adams, J., Aguilar, J., Ahlers, M., Ahrens, M., Alispach, C., Andeen, K., Anderson, T., Ansseau, I., et al., 2020. Time-integrated neutrino source searches with 10 years of icecube data. *Physical review letters* 124, 051103.
- Abbasi, R., Ackermann, M., Adams, J., Agarwalla, S., Aggarwal, N., Aguilar, J., Ahlers, M., Alameddine, J., Amin, N., Andeen, K., et al., 2023a. Limits on neutrino emission from grb 221009a from mev to pev using the icecube neutrino observatory. *The Astrophysical Journal Letters* 946, L26.
- Abbasi, R., Ackermann, M., Adams, J., Agarwalla, S., Aguilar, J., Ahlers, M., Alameddine, J., Amin, N., Andeen, K., Anton, G., et al., 2023b. Icecat-1: The icecube event catalog of alert tracks. *The Astrophysical Journal Supplement Series* 269, 25.
- Abbasi, R., Ackermann, M., Adams, J., Aguilar, J., Ahlers, M., Ahrens, M., Alameddine, J., Alves, A., Amin, N., Andeen, K., et al., 2022. Searches for neutrinos from gamma-ray bursts using the icecube neutrino observatory. *The Astrophysical Journal* 939, 116.
- Abbasi, R., Ackermann, M., Adams, J., Aguilar, J., Ahlers, M., Ahrens, M., Alispach, C., Alves Jr, A., Amin, N., Andeen, K., et al., 2021. Icecube high-energy starting event sample: Description and flux characterization with 7.5 years of data. *Physical Review D* 104, 022002.
- Abe, K., Abe, S., Abhishek, A., Acero, F., Aguasca-Cabot, A., Agudo, I., Alispach, C., Ambrosino, D., Ambrosino, F., Antonelli, L., et al., 2025. Grb 221009a: Observations with ISt-1 of ctao and implications for structured jets in long gamma-ray bursts. *The Astrophysical Journal Letters* 988, L42.
- Adriani, O., Albert, A., Alhebsi, A., Alshalloudi, S., Alshamsi, M., Garre, S.A., Ambrosone, A., Ameli, F., Andre, M., Aphecetche, L., et al., 2025. Constraining gamma-ray burst parameters with the first ultra-high energy neutrino event km3-230213a. arXiv preprint arXiv:2509.14895 .
- Ai, S., Gao, H., 2023. Model constraints based on the icecube neutrino nondetection of grb 221009a. *The Astrophysical Journal* 944, 115.
- Aiello, S., Akrame, S., Ameli, F., Anassontzis, E., Andre, M., Androulakis, G., Anghinolfi, M., Anton, G., Ardid, M., Aublin, J., et al., 2019. Sensitivity of the km3net/orca neutrino telescope to point-like neutrino sources. *Astroparticle Physics* 111, 100–110.
- Aiello, S., Albert, A., Alshamsi, M., Garre, S.A., Ambrosone, A., Ameli, F., André, M., Androutsou, E., Angueta, M., Aphecetche, L., et al., 2024. Search for neutrino emission from grb 221009a using the km3net arca and orca detectors. *Journal of Cosmology and Astroparticle Physics* 2024, 006.
- Álvarez-Muñiz, J., Alves Batista, R., Balagopal V, A., Bolmont, J., Bustamante, M., Carvalho Jr, W., Charrier, D., Cognard, I., Decoene, V., Denton, P.B., et al., 2020. The giant radio array for neutrino detection (grand): Science and design. *Science China Physics, Mechanics & Astronomy* 63, 219501.
- Banerjee, B., Macera, S., De Santis, A.L., Mei, A., Tissino, J., Oganessian, G., Frederiks, D.D., Lysenko, A.L., Svinkin, D.S., Tsvetkova, A.E., et al., 2025. Observation of the spectral turnover in the afterglow emission of grb 221009a. *Astronomy & Astrophysics* 701, A68.
- Barnard, M., Ghosh, A., Joshi, J.C., Razzaque, S., 2025. Modelling multiwavelength afterglows of the vhe-grb population. *Monthly Notices of the Royal Astronomical Society* 543, 4218–4234.
- Blandford, R., McKee, C., 1976. Fluid dynamics of relativistic blast waves. *The physics of Fluids* 19, 1130–1138.

- Burgess, J.M., Bégué, D., Greiner, J., Giannios, D., Bacelj, A., Berlato, F., 2020. Gamma-ray bursts as cool synchrotron sources. *Nature Astronomy* 4, 174–179. doi:10.1038/s41550-019-0911-z, arXiv:1810.06965.
- Chiang, J., Dermer, C.D., 1999. Synchrotron and synchrotron self-compton emission and the blast-wave model of gamma-ray bursts. *The Astrophysical Journal* 512, 699.
- Costa, E., Frontera, F., Heise, J., Feroci, M., in't Zand, J., Fiore, F., Cinti, M.N., Dal Fiume, D., Nicastro, L., Orlandini, M., Palazzi, E., Rapisarda, M., Zavattini, G., Jager, R., Parmar, A., Owens, A., Molendi, S., Cusumano, G., Maccarone, M.C., Giarrusso, S., Coletta, A., Antonelli, L.A., Giommi, P., Muller, J.M., Piro, L., Butler, R.C., 1997. Discovery of an X-ray afterglow associated with the γ -ray burst of 28 February 1997. *Nature* 387, 783–785. doi:10.1038/42885, arXiv:astro-ph/9706065.
- de Ugarte Postigo, A., Izzo, L., Pugliese, G., Xu, D., Schneider, B., Fynbo, J.P.U., Tanvir, N.R., Malesani, D.B., Saccardi, A., Kann, D.A., Wiersema, K., Gompertz, B.P., Thoene, C.C., Levan, A.J., Stargate Collaboration, 2022. GRB 221009A: Redshift from X-shooter/VLT. *GRB Coordinates Network* 32648, 1.
- Derishev, E., Piran, T., 2019. The physical conditions of the afterglow implied by magic's sub-teV observations of grb 190114c. *The Astrophysical Journal Letters* 880, L27.
- Dermer, C.D., Chiang, J., Mitman, K.E., 2000. Beaming, baryon loading, and the synchrotron self-compton component in gamma-ray bursts. *The Astrophysical Journal* 537, 785.
- Dominguez, A., Primack, J.R., Rosario, D., Prada, F., Gilmore, R., Faber, S., Koo, D., Somerville, R., Pérez-Torres, M., Pérez-González, P., et al., 2011. Extragalactic background light inferred from aegis galaxy-sed-type fractions. *Monthly Notices of the Royal Astronomical Society* 410, 2556–2578. doi:10.1111/j.1365-2966.2010.17631.x.
- Foffano, L., Tavani, M., Piano, G., 2024. Theoretical modeling of the exceptional grb 221009a afterglow. *The Astrophysical Journal Letters* 973, L44.
- Foreman-Mackey, D., Hogg, D.W., Lang, D., Goodman, J., 2013. emcee: the mcmc hammer. *Publications of the Astronomical Society of the Pacific* 125, 306.
- Fraija, N., Duran, R.B., Dichiaro, S., Beniamini, P., 2019. Synchrotron self-compton as a likely mechanism of photons beyond the synchrotron limit in grb 190114c. *The Astrophysical Journal* 883, 162.
- Frail, D.A., Kulkarni, S.R., Nicastro, L., Feroci, M., Taylor, G.B., 1997. The radio afterglow from the γ -ray burst of 8 May 1997. *Nature* 389, 261–263. doi:10.1038/38451.
- Frederiks, D., Svinkin, D., Lysenko, A., Molkov, S., Tsvetkova, A., Ulanov, M., Ridnaia, A., Lutovinov, A., Lapshov, I., Tkachenko, A., et al., 2023. Properties of the extremely energetic grb 221009a from konus-wind and srg/art-xc observations. *The Astrophysical Journal Letters* 949, L7.
- Gao, H., Lei, W.H., Wu, X.F., Zhang, B., 2013. Compton scattering of self-absorbed synchrotron emission. *Monthly Notices of the Royal Astronomical Society* 435, 2520–2531.
- Gehrels, N., 1986. Confidence limits for small numbers of events in astrophysical data. *Astrophysical Journal, Part 1 (ISSN 0004-637X)*, vol. 303, April 1, 1986, p. 336-346. 303, 336–346.
- Geng, J.J., Zhang, Y.K., Gao, H.X., Xu, F., Li, B., Sun, T.R., Wang, A.L., Xu, Z.J., Liu, Y.Q., Yang, J., et al., 2025. Spreading and multi-wavelength emissions of an ultra-narrow relativistic jet from grb 221009a. arXiv preprint arXiv:2503.17765 .
- Gill, R., Granot, J., 2023. Grb 221009a afterglow from a shallow angular structured jet. *Monthly Notices of the Royal Astronomical Society: Letters* 524, L78–L83.
- Gottlieb, O., Nakar, E., Piran, T., 2018. The cocoon emission—an electromagnetic counterpart to gravitational waves from neutron star mergers. *Monthly Notices of the Royal Astronomical Society* 473, 576–584.
- Gould, R.J., Schröder, G.P., 1967. Pair production in photon-photon collisions. *Physical Review* 155, 1404.
- HESS Collaboration, 2019. A very-high-energy component deep in the γ -ray burst afterglow. *Nature* 575, 464–467.
- HESS Collaboration, 2021. Revealing x-ray and gamma ray temporal and spectral similarities in the grb 190829a afterglow. *Science* 372, 1081–1085.
- Huang, Y., Hu, S., Chen, S., Zha, M., Liu, C., Yao, Z., Cao, Z., et al., 2022. Lhaaso observed grb 221009a with more than 5000 vhe photons up to around 18 tev. *GRB Coordinates Network* 32677, 1.
- IceCube Collaboration, 2022. GRB 221009A: Upper limits from a neutrino search with IceCube. *GRB Coordinates Network* 32665, 1.
- Isravel, H., Pe'er, A., Bégué, D., 2023. Proton synchrotron origin of the very-high-energy emission of grb 190114c. *The Astrophysical Journal* 955, 70.
- Jacovich, T.E., Beniamini, P., Van Der Horst, A.J., 2021. Modelling synchrotron self-compton and Klein–Nishina effects in gamma-ray burst afterglows. *Monthly Notices of the Royal Astronomical Society* 504, 528–542.
- Joshi, J.C., Razzaque, S., 2021. Modelling synchrotron and synchrotron self-compton emission of gamma-ray burst afterglows from radio to very-high energies. *Monthly Notices of the Royal Astronomical Society* 505, 1718–1729.
- KM3NeT Collaboration, 2022. GRB 221009A: search for neutrinos with KM3NeT. *GRB Coordinates Network* 32741, 1.

- Kusafuka, Y., Asano, K., 2025. Tev afterglow of boat grb without jet break. *Monthly Notices of the Royal Astronomical Society* 540, 2098–2101.
- Lamb, G.P., Kobayashi, S., 2017. Electromagnetic counterparts to structured jets from gravitational wave detected mergers. *Monthly Notices of the Royal Astronomical Society* 472, 4953–4964.
- Lazzati, D., Perna, R., Morsony, B.J., Lopez-Camara, D., Cantiello, M., Ciolfi, R., Giacomazzo, B., Workman, J.C., 2018. Late time afterglow observations reveal a collimated relativistic jet in the ejecta of the binary neutron star merger gw170817. *Physical Review Letters* 120, 241103.
- Lesage, S., Veres, P., Briggs, M., Goldstein, A., Kocevski, D., Burns, E., Wilson-Hodge, C., Bhat, P., Huppenkothen, D., Fryer, C., et al., 2023. Fermi-gbm discovery of grb 221009a: An extraordinarily bright grb from onset to afterglow. *The Astrophysical Journal Letters* 952, L42.
- LHAASO collaboration, 2023. Very high-energy gamma-ray emission beyond 10 tev from grb 221009a. *Science Advances* 9, eadj2778.
- LHAASO Collaboration, CAO, Z., Aharonian, F., An, Q., Axikegu, Bai, L., Bai, Y., Bao, Y., Bastieri, D., Bi, X., et al., 2023. A tera-electron volt afterglow from a narrow jet in an extremely bright gamma-ray burst. *Science* 380, 1390–1396.
- Lloyd, N.M., Petrosian, V., 2000. Synchrotron Radiation as the Source of Gamma-Ray Burst Spectra. *Astrophysical Journal* 543, 722–732. doi:10.1086/317125, arXiv:astro-ph/0007061.
- MAGIC Collaboration, 2019. Observation of inverse compton emission from a long γ -ray burst. *Nature* 575, 459–463. URL: <https://doi.org/10.1038/s41586-019-1754-6>, doi:10.1038/s41586-019-1754-6.
- MAGIC Collaboration, 2024. Magic detection of grb 201216c at $z=1.1$. *Monthly Notices of the Royal Astronomical Society* 527, 5856–5867.
- Margutti, R., Berger, E., Fong, W.f., Guidorzi, C., Alexander, K., Metzger, B., Blanchard, P., Cowperthwaite, P., Chornock, R., Eftekhari, T., et al., 2017. The electromagnetic counterpart of the binary neutron star merger ligo/virgo gw170817. v. rising x-ray emission from an off-axis jet. *The Astrophysical Journal Letters* 848, L20.
- Mészáros, P., Rees, M.J., 1997. Optical and Long-Wavelength Afterglow from Gamma-Ray Bursts. *Astrophysical Journal* 476, 232–237. doi:10.1086/303625, arXiv:astro-ph/9606043.
- Mondal, T., Chakraborty, S., Resmi, L., Bose, D., 2025. Follow-up of neutron star mergers with cta and prospects for joint detection with gravitational-wave detectors. *The Astrophysical Journal* 983, 35.
- Mondal, T., Pramanick, S., Resmi, L., Bose, D., 2023. Probing gamma-ray burst afterglows with the cherenkov telescope array. *Monthly Notices of the Royal Astronomical Society* 522, 5690–5700.
- Mooley, K., Nakar, E., Hotokezaka, K., Hallinan, G., Corsi, A., Frail, D., Horesh, A., Murphy, T., Lenc, E., Kaplan, D., et al., 2018. A mildly relativistic wide-angle outflow in the neutron-star merger event gw170817. *Nature* 554, 207–210.
- Murase, K., 2007. High energy neutrino early afterglows from gamma-ray bursts revisited. *Physical Review D—Particles, Fields, Gravitation, and Cosmology* 76, 123001.
- Murase, K., Mukhopadhyay, M., Kheirandish, A., Kimura, S.S., Fang, K., 2022. Neutrinos from the brightest gamma-ray burst? *The Astrophysical Journal Letters* 941, L10.
- Murase, K., Toma, K., Yamazaki, R., Mészáros, P., 2011. On the implications of late internal dissipation for shallow-decay afterglow emission and associated high-energy gamma-ray signals. *The Astrophysical Journal* 732, 77.
- Nakar, E., Ando, S., et al., 2009. Klein–nishina effects on optically thin synchrotron and synchrotron self-compton spectrum. *The Astrophysical Journal* 703, 675.
- O’Connor, B., Troja, E., Ryan, G., Beniamini, P., Van Eerten, H., Granot, J., Dichiara, S., Ricci, R., Lipunov, V., Gillanders, J.H., et al., 2023. A structured jet explains the extreme grb 221009a. *Science Advances* 9, eadi1405.
- Piran, T., Narayan, R., et al., 1998. Spectra and light curves of gamma-ray burst afterglows. *The Astrophysical Journal* 497, L17.
- Razzaque, S., 2010. A leptonic–hadronic model for the afterglow of gamma-ray burst 090510. *The Astrophysical Journal Letters* 724, L109.
- Razzaque, S., 2013. Long-lived pev–eev neutrinos from gamma-ray burst blastwave. *Physical Review D—Particles, Fields, Gravitation, and Cosmology* 88, 103003.
- Razzaque, S., Yang, L., 2015. Pev-eev neutrinos from grb blast waves in icecube and future neutrino telescopes. *Physical Review D* 91, 043003.
- Ren, J., Wang, Y., Dai, Z.G., 2024a. Jet structure and burst environment of grb 221009a. *The Astrophysical Journal* 962, 115.
- Ren, J., Wang, Y., Dai, Z.G., 2024b. Jet structure and burst environment of grb 221009a. *The Astrophysical Journal* 962, 115. URL: <https://dx.doi.org/10.3847/1538-4357/ad1bcd>, doi:10.3847/1538-4357/ad1bcd.
- Resmi, L., Schulze, S., Ishwara-Chandra, C., Misra, K., Buchner, J., De Pasquale, M., Sánchez-Ramírez, R., Klose, S., Kim, S., Tanvir, N., et al., 2018. Low-frequency view of gw170817/grb 170817a with the giant metrewave radio telescope. *The Astrophysical Journal* 867, 57.

- Sahu, S., Polanco, I.A.V., Rajpoot, S., 2022. Very high-energy afterglow emission of grb 190829a: Evidence for its hadronic origin? *The Astrophysical Journal* 929, 70.
- Salmonson, J.D., 2003. Perspective on afterglows: numerically computed views, light curves, and the analysis of homogeneous and structured jets with lateral expansion. *The Astrophysical Journal* 592, 1002.
- Sari, R., Esin, A.A., 2001. On the synchrotron self-compton emission from relativistic shocks and its implications for gamma-ray burst afterglows. *The Astrophysical Journal* 548, 787.
- Sari, R., Piran, T., Halpern, J., 1999. Jets in grbs. arXiv preprint astro-ph/9903339 .
- Sari, R., Piran, T., Narayan, R., 1998. Spectra and Light Curves of Gamma-Ray Burst Afterglows. *Astrophysical Journal* 497, L17–L20. doi:10.1086/311269, arXiv:astro-ph/9712005.
- Sari, R., Piran, T., Narayan, R., 1998. Spectra and light curves of gamma-ray burst afterglows. *The Astrophysical Journal* 497, L17–L20. URL: <https://doi.org/10.1086/311269>, doi:10.1086/311269.
- Sato, Y., Murase, K., Ohira, Y., Yamazaki, R., 2023. Two-component jet model for multiwavelength afterglow emission of the extremely energetic burst grb 221009a. *Monthly Notices of the Royal Astronomical Society: Letters* 522, L56–L60.
- Svinkin, D., Frederiks, D., Ridnaia, A., Lysenko, A., Cline, T., Konus-Wind Team, von Kienlin, A., Zhang, X., Rau, A., Savchenko, V., Bozzo, E., Ferrigno, C., INTEGRAL SPI-ACS Team, Goldstein, A., Briggs, M.S., Wilson-Hodge, C., Fermi Gbm Team, Barthelmy, S., Cummings, J., Krimm, H., Palmer, D., Tohuvavohu, A., Swift-Bat Team, 2022. IPN triangulation of extremely bright GRB 221009A. *GRB Coordinates Network* 32641, 1.
- van Paradijs, J., Groot, P.J., Galama, T., Kouveliotou, C., Strom, R.G., Telting, J., Rutten, R.G.M., Fishman, G.J., Meehan, C.A., Pettini, M., Tanvir, N., Bloom, J., Pedersen, H., Nørregaard-Nielsen, H.U., Linden-Vørnle, M., Melnick, J., Van der Steene, G., Bremer, M., Naber, R., Heise, J., in't Zand, J., Costa, E., Feroci, M., Piro, L., Frontera, F., Zavatini, G., Nicastro, L., Palazzi, E., Bennett, K., Hanlon, L., Parmar, A., 1997. Transient optical emission from the error box of the γ -ray burst of 28 February 1997. *Nature* 386, 686–689. doi:10.1038/386686a0.
- Veres, P., Burns, E., Bissaldi, E., Lesage, S., Roberts, O., Team, F.G., et al., 2022. Grb 221009a: Fermi gbm detection of an extraordinarily bright grb. *GRB Coordinates Network* 32636, 1.
- Veres, P., Fraija, N., Lesage, S., Goldstein, A., Briggs, M., Bhat, P., 2024. Non-detection of neutrinos from the boat: Improved constraints on the parameters of grb 221009a. arXiv preprint arXiv:2408.16748 .
- Vietri, M., 1995. On the acceleration of ultra high energy cosmic rays in gamma ray bursts. arXiv preprint astro-ph/9506081 .
- Wang, X.Y., Liu, R.Y., Zhang, H.M., Xi, S.Q., Zhang, B., 2019. Synchrotron self-compton emission from external shocks as the origin of the sub-tev emission in grb 180720b and grb 190114c. *The Astrophysical Journal* 884, 117.
- Waxman, E., 1995. Cosmological gamma-ray bursts and the highest energy cosmic rays. *Physical Review Letters* 75, 386.
- Waxman, E., Bahcall, J., 1997. High energy neutrinos from cosmological gamma-ray burst fireballs. *Physical Review Letters* 78, 2292.
- Waxman, E., Bahcall, J.N., 2000. Neutrino afterglow from gamma-ray bursts: $\sim 10^{18}$ ev. *The Astrophysical Journal* 541, 707.
- Wijers, R., Galama, T., 1999. Physical parameters of grb 970508 and grb 971214 from their afterglow synchrotron emission. *The Astrophysical Journal* 523, 177.
- Williams, M.A., Kennea, J.A., Dichiara, S., Kobayashi, K., Iwakiri, W.B., Beardmore, A.P., Evans, P.A., Heinz, S., Lien, A., Oates, S.R., et al., 2023. Grb 221009a: discovery of an exceptionally rare nearby and energetic gamma-ray burst. *The Astrophysical Journal Letters* 946, L24.
- Zhang, B., 2018. *The physics of gamma-ray bursts*. Cambridge University Press.
- Zhang, B., Wang, X.Y., Zheng, J.H., 2024. The boat grb 221009a: A poynting-flux-dominated narrow jet surrounded by a matter-dominated structured jet wing. *Journal of High Energy Astrophysics* 41, 42–53.
- Zheng, J.H., Wang, X.Y., Liu, R.Y., Zhang, B., 2024. A narrow uniform core with a wide structured wing: Modeling the tev and multiwavelength afterglows of grb 221009a. *The Astrophysical Journal* 966, 141.